Scalable additive manufacturing via integral image formation

Seok Kim
Massachusetts Institute of Technology
Jordan Handler
Massachusetts Institute of Technology
Young Tae Cho
Changwon National University
George Barbastathis
Massachusetts Institute of Technology
Nicholas Fang (nicfang@mit.edu)
Massachusetts Institute of Technology

Article

Keywords: microarchitectures, microstructures, integral lithography technique

Posted Date: October 6th, 2020

DOI: https://doi.org/10.21203/rs.3.rs-85511/v1

Scalable additive manufacturing via integral image formation

Seok Kim[1,2], Jordan Jerome Handler[3], Young Tae Cho[2], George Barbastathis[1,4],

and Nicholas Xuanlai Fang[1]*

[1]Department of Mechanical Engineering, Massachusetts Institute of Technology, Cambridge, MA 02139, USA.

[2]Department of Mechanical Engineering, Changwon National University, Changwon, South Korea.

[3]Sloan School of Management, Massachusetts Institute of Technology, Cambridge, MA 02142 USA.

[4]Singapore-MIT Alliance for Research and Technology (SMART) Centre, 1 Create Way, Singapore 138602.

*e-mail: nicfang@mit.edu

Abstract

Additive manufacturing techniques are used to fabricate functional microstructures with customised mechanical and chemical properties. One common technique is projection microstereolithography, which has recently been developed to support smaller features, larger build areas, and/or faster speeds. The limitation of such systems is that they typically utilise a single-aperture imaging configuration, which restricts their ability to produce microstructures in large volumes owing to the tradeoff between image resolution and image field area. In this paper, we propose an integral lithography technique based on integral image reconstruction coupled with a planar lens array. The individual microlenses in the planar lens array maintain a high numerical aperture and are employed to create digital light patterns that can expand the printable area by the number of microlenses (10^3-10^4). The proposed lens array-based integral imaging system can simultaneously scale up and scale down incoming image fields, thereby allowing for the scalable stereolithographic fabrication of three-dimensional features that surpass the resolution-to-area scaling limit. We extend the printing capability of integral lithography to fabricate deterministic

nonperiodic structures through the rotational overlapping or stacking of multiple exposures with controlled angular offsets. The proposed system provides new possibilities for producing periodic and deterministic aperiodic microarchitectures spanning four orders of magnitude from micrometres to centimetres. These microarchitectures can be applied to biological scaffolds, chemical reactors, functional surfaces, and metastructures.

Introduction

Rapid developments in the fabrication of three-dimensional (3D) printed architectures has revolutionised the production of functional structures for mechanical/acoustic metamaterials [1-3], cellular mechanobiological materials [4], and structures for energy/environmental applications [5, 6]. For instance, 3D microstructures with mechanically compliant materials and customised constructed scaffolds offer tailored functionality for biocompatibility and defined stiffness [4]. Moreover, the application of functional structures in catalytic systems has improved efficiencies by utilising microscale- and nanoscale architectures designed to increase surface area-to-volume ratios with reduced mass [5, 6]. Furthermore, advances in additive manufacturing techniques have allowed for the fabrication of functional structures with complex architectures at various spatial scales down to the sub-micrometre scale [7-10]. The commonly used stereolithography technique supports the fabrication of high resolution and geometrically complex products [7, 8], and recent advances have significantly improved feature resolution [11, 12], speed [13], and build size [14-17]. For instance, digital micro-mirror devices [11] and spatial light modulators [14] can be utilised to cure large areas (termed projection micro-stereolithography (PμSL)), as opposed to the conventional 'tracing' approach employed by single or multiple spot laser systems [18]. Recent works have demonstrated the variants of PμSL that incorporate a serial printing process in which many repeated scanning cycles expand the overall build size without sacrificing resolution [14-17]. One recent derivative of PμSL, named volumetric printing, overcomes the current layer-by-layer manufacturing approach to fabricate 3D objects almost instantaneously [19, 20].

However, despite these system improvements, conventional PμSL methods use an imaging platform that relies on a single-aperture imaging system in which an incoming image is focused directly onto a single planar area. Consequently, the amount of transferred spatial information is fundamentally limited by the space–bandwidth product (SBP) of the pixelated digital projection system. The SBP is defined as the number of pixels required to realise the maximum information capacity. The SBP of a conventional PμSL platform is typically in the megapixels (Mpx) range regardless of the numerical aperture (***NA***) or magnification (***M***) of imaging optics. This results in a tradeoff between the achievable feature resolution and the total image area [8, 21]. This tradeoff must be eliminated to further advance microstructural 3D printing for use in production.

This problem can potentially be solved by utilizing an image multiplication strategy (i.e., numbering-up) in conjunction with a planar microoptical imaging system. With continued advances in low-cost and large scale microlens array fabrication techniques, microoptical devices have become a promising tool for large-area display applications such as integral imaging 3D displays [22]. A benefit of these fabrication techniques is that they are scalable. Image multiplication via microoptical imaging devices has been demonstrated in Talbot array illumination [23] and microlens projection lithography [24], which are capable of fabricating sub-micrometre two-dimensional (2D) lattice structures. However, the use of a static photomask limits the imaging function to a simple duplication of a single object, and therefore, it does not satisfy the design requirements for complex architectures with multiple layers beyond 2D planar structures.

At present, microoptical and single-aperture imaging systems require further development and no existing technologies can support a scalable SBP in additive manufacturing. In this work, we propose a new stereolithographic printing system that utilises integral image formation by a planar microoptical device to provide a scalable additive manufacturing method without requiring serial scanning. The proposed engineered projection system is based on a lens array, in which each microlens can maintain a high ***NA*** and the overall print area can be increased with the number of microlenses. The microoptical device combined with digital light processing allows for a scalable reconstruction of projected output images via the parallel transfer, superposition, and integration of incoming images. The imaging mechanism is described using a simple thin-lens equation that predicts the complex output patterns of the lens array using simple inputs. In addition, we develop an integral lithography approach, in which the reconstructed patterns obtained from the integral imaging of multiple incoming images are used to improve the scalability of the print area and provide it with a more uniform light distribution. We evaluate the scalability of the approach and its ability to increase print areas by 10^2–10^3 times compared to current commercial systems, which translates to an SBP of 0.1–0.28 gigapixels (Gpx). Periodic microarchitectures spanning four orders of magnitude from the micrometer scale to centimeter scale are produced. In addition, we demonstrate the extended printing capability of integral lithography to create deterministic aperiodic structures through the rotational stacking of multiple integral projections with controlled angular offsets.

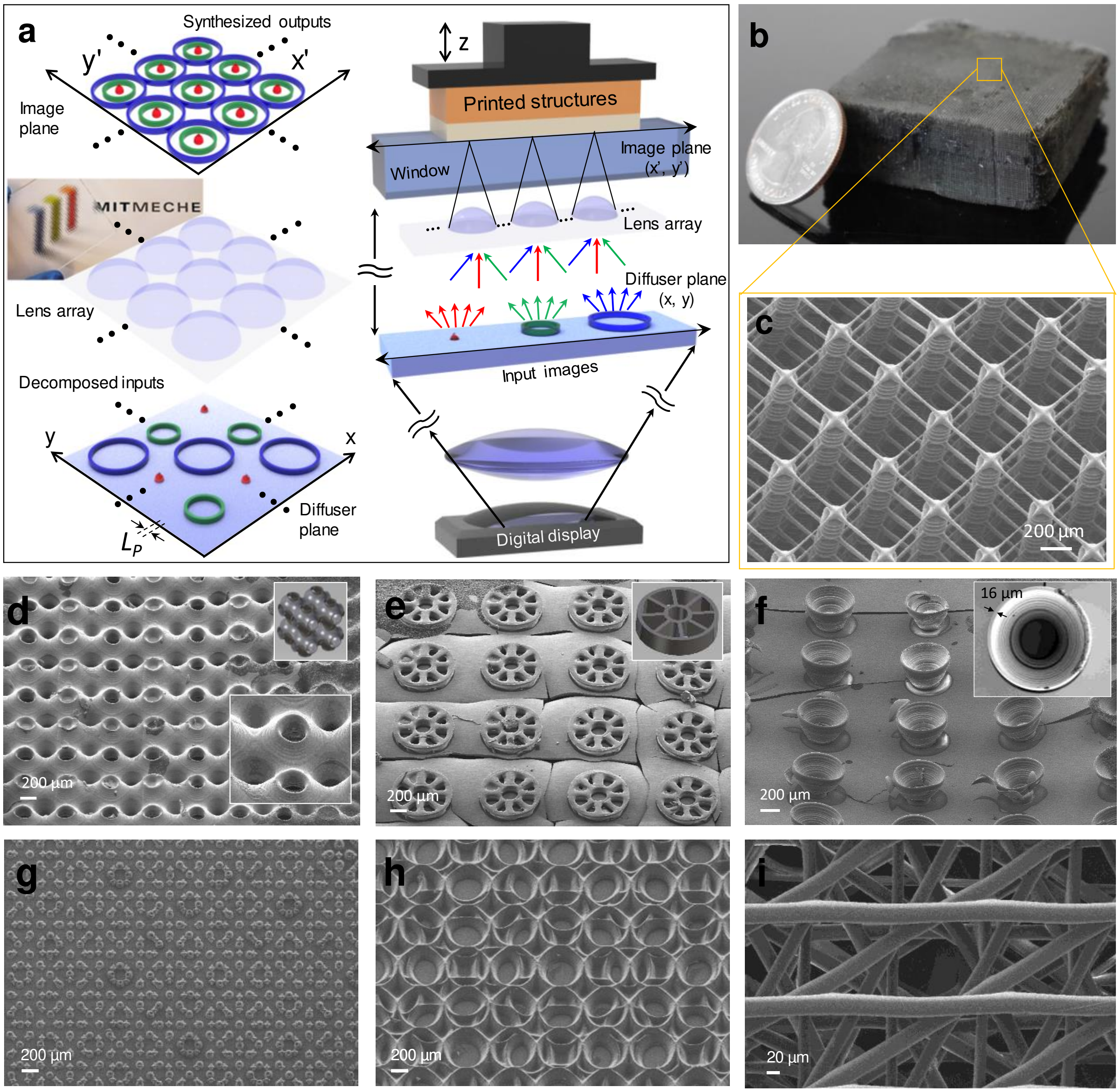

Fig. 1: Integral lithographic system for scalable additive manufacturing. (A) Schematic of the integral lithographic system. The reconstructed imaging patterns are projected by the lens array (displayed in front of the MIT mechanical logo) in conjunction with the digital microdisplay. (B to F) Periodic microstructures were fabricated via linear stacking during layer-by-layer printing with an exposure time 3-30 s at an intensity of 33 mW/cm^2. These multiscale structures were produced by the lens array (Lens 1, defined in the caption of Fig. 4 and the Methods section): (B) cubic-truss microlattices (400 layers with a polymerisation thickness of 5–50 μm), (C) scanning electron micrograph of microlattices with strut

suspended beam diameter of 5 μm; (D) triply periodic bicontinuous structures (60 layers with a polymerisation thickness of 20 μm); (E) circular-lattice microscaffolds (10 layers with a polymerisation thickness of 10 μm); (F) trapezoidal shell-type microstructures with a reentrant geometry (20 layers with a polymerisation thickness of 20 μm). (G to I) Nonperiodic microstructures created via rotational stacking with precisely controllable angular offsets during layer-by-layer printing. These structures were fabricated by a lens array (Lens 2, defined in the caption of Fig. 4 and the Methods section): (G) 8-fold quasi-lattices with hetero sublattices and (H) identical sublattices; (I) deterministic aperiodic woodpile lattices stacked at an angle of $2\pi/12$ with a linear angular sequence.

Results

Engineered imaging system: A schematic overview of the proposed 3D printing system is shown in Fig. 1A. A digitally generated object image is projected onto a diffuser, which acts as the input image plane, and observed by a lens array [24-26]. The lens array (displayed in Fig. 1A in front of the MIT MechE logo) focuses light sources from multiple viewpoints to replicate and reconstruct images into new patterns [27, 28]. This functionality enables incoming images to be superimposed and integrally reconstructed. The engineered projection-based printing system allows for the high-resolution and scalable stereolithographic manufacturing of complex microstructures by utilizing the versatile imaging functions in conjunction with the lens array with the microdisplay device. During the printing process, multiple output images, each of which is generated by a unit-lens of the lens array, form reconfigurable synthetic patterns via one or more combinations of replication, superposition, and integral reconstruction. Then a set of these reconstructed images is used to create 3D architectures via linear or rotational stacking during layer-by-layer printing. The prints of the complex 3D microstructures are shown in Fig. 1B-I and S1. The minimum feature sizes of these microstructures are ~ 5–20 μm, and their areas are several tens of square centimetres. The microstructures demonstrate the feasibility of printing polymeric structures that exceed the resolution-to-area scaling limit. The microlattices shown in Fig. 1B-C are fabricated using 400 layers of reconstructed output patterns and a polymerisation layer thickness of 5–50 μm. The cubic-truss lattice shown in these figures is composed of three freestanding mesh layers that are suspended on an array of vertical posts and separated by identical distances in the vertical direction. These polymeric microlattices can be utilised at scale in customised mechanical environments, such as to mimic artificial axons [4] or form a catalytic reactor with a high surface area-to-volume ratio [29]. Our approach allows for the fabrication of complex 3D microstructures that are difficult to fabricate using conventional projection lithography processes. For example, we 3D print a wide variety of structures by varying the geometric overlap of the image outputs from each unit lens. The printed structures range from interconnected bicontinuous structures (Fig. 1D) to isolated microarchitectures of circular-lattice scaffolds (Fig. 1E) and trapezoidal re-entrant structures (Fig. 1F). These examples of complex 3D microstructures with different degrees of connectivity can be extended to a variety of tissue scaffolds [30], mechanical metamaterials [31], feed spacers for water reuse system [32], or functional surfaces [33]. In addition to the periodic microstructures in Fig. 1B-F, our approach allows for the fabrication of aperiodic microstructures based on broken lattice-dependent symmetry (Fig. 1G-I) with different degrees of periodicity. Aperiodic microstructures can be used to create exotic metasurfaces or woodpile structures for wave engineering [34-36].

Figure 2 shows how the imaging mechanism manipulates the projected output patterns, and Fig. 2A shows the geometric relationship between the lens array, input image, and output image. The input image information is transferred in parallel by the lens array to generate an array of repetitive patterns that can produce complex patterns beyond simple replicated images. The relationship between the input image size, $\boldsymbol{a}$, the output image size, $\boldsymbol{a'}$, and the overlap of resulting output images is given by the simple thin-lens equation: $1/\boldsymbol{f} = 1/\boldsymbol{b} + 1/\boldsymbol{b'}$ [37], where $\boldsymbol{f}$ is the effective focal length of the unit-lens, $\boldsymbol{b}$ is the distance between the lens array and input image plane, and $\boldsymbol{b'}$ is the distance between the lens array and the output image plane. The demagnification factor of the output image from each unit lens is defined as $\boldsymbol{D} = \boldsymbol{b'}/\boldsymbol{b} = \boldsymbol{f}/(\boldsymbol{b} - \boldsymbol{f})$, and the resulting $\boldsymbol{a'}$ of each unit lens is $\boldsymbol{a} \times \boldsymbol{D}$, as shown in Fig. 2A. The lens array is mounted on a microtranslation stage, which allows for longitudinal movement along the z-axis to control the $\boldsymbol{D}$ of the output image by adjusting $\boldsymbol{b}$ from the input image plane. Note that we assume that the size of the unit lens is equal to the lattice spacing, $\boldsymbol{p}$, of the lens array. When $\boldsymbol{a'}$ is larger than $\boldsymbol{p}$, the multiplied images interconnect and overlap with each other to reproduce interwoven patterns in the same imaging plane (see Fig. S2-4 in Supplementary Information fir details).

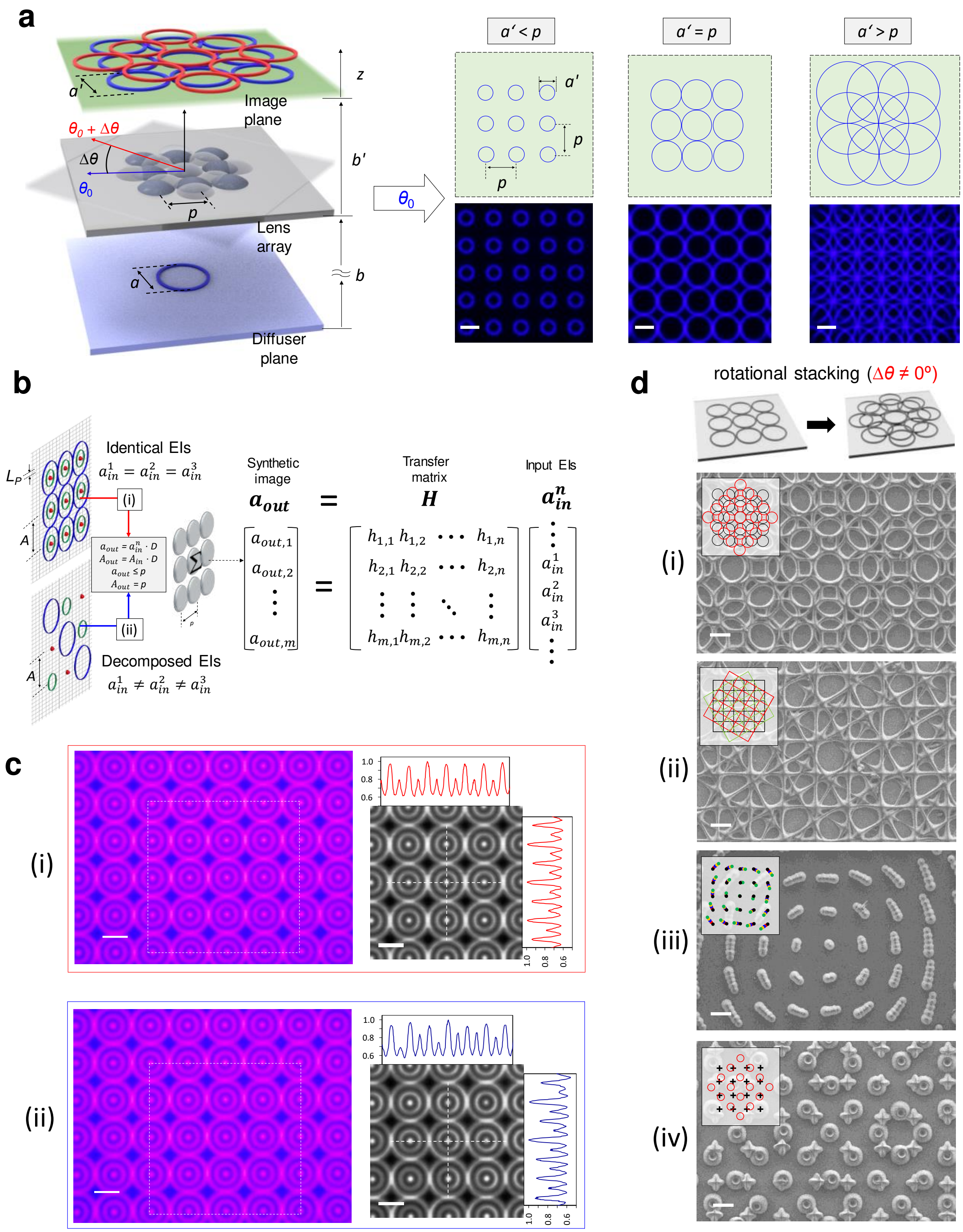

157

158 **Fig. 2: Digitally controlled imaging patterns.** (A) The geometric relationship between the lens array and

an input object produces kaleidoscopic interwoven patterns. The synthetic images are projected on an imaging plane of the lens array (Lens 2), and captured by an optical microscope. Parallel replication of a single object image by the lens array, which captures an object image and generates an array of repetitive patterns ($\boldsymbol{a'}/\boldsymbol{p} < 1$). Interwoven patterns form through the overlap and superposition of multiple replicated images based on the interaction between the lens array and a single object image ($\boldsymbol{a'}/\boldsymbol{p} \geq 1$). The scale bars are 100 μm. (B to C) Integral imaging patterns with compressive multi-projection: (B) matrix form of the integral image formation between input objects of identical/decomposed EIs and projected outputs. Transfer matrix $\boldsymbol{H}$ is determined by its elements, $\boldsymbol{h}_{m,n}$, which represent the impulse response function of the unit lens in the lens array. $\boldsymbol{m}$ and $\boldsymbol{n}$ represent the numbers of unit lenses in the lens array in the horizontal and vertical directions, respectively; (C) optical-microscope-captured topologies and cross-sectional intensity profiles of integral imaging patterns created by a digital microdisplay with a projected pixel size ($\boldsymbol{L_P}$) of 50 μm. The intensity profiles were normalised to the maximum grey value versus the pixel distance. (i) and (ii) show integral imaging patterns with the identical EIs and three decomposed EIs, respectively, of the concentric circular grating on the imaging plane through the lens array. (D) Aperiodic lattices with rotational symmetries via multiple integral projections. Broken lattice-dependent symmetry of (i) quasilattices with identical bilayer (angular offset: 45°), (ii-iii) superlattices with identical trilayer (angular offsets: ± 30°) and multilayer (angular offsets: 3°), and (iv) incommensurate Moiré lattices with hetero multilayer (angular offset: 45°). These structures were printed using Lens 2. The scale bars are 100 μm.

The homogeneous light distribution on the lens array from the diffuser enables images from different perspectives (i.e. not orthogonally projected) to be combined in the reconstruction process [24, 26]. In contrast to the patterns generate based on the parallel transfer and superposition of a single input image, as shown in Fig. 2A, these synthetic patterns are created by imaging techniques that are analogous to the integral imaging techniques used in a multiview 3D display

[25]. Each unit lens of the lens array can observe multiple elemental images (EIs) and reconstruct them into identical and/or highly periodic composited patterns, as shown in Fig. 2B-C. To describe the relationship between the elements of the input objects and output images, we consider the optical system of a one-dimensional model with column vectors $\boldsymbol{a}_{in}^{n}$ and $\boldsymbol{a}_{out}$ and optical system matrix $\boldsymbol{H}$, where $\boldsymbol{a}_{in}^{n}$ and $\boldsymbol{a}_{out}$ are the elements of the input objects and the projected images, respectively, (see the Methods section). Then, the system can be described as $[\boldsymbol{a}_{out}] = [\boldsymbol{H}][\boldsymbol{a}_{in}^{n}]$, as shown in Fig. 2B. The spacing, $\boldsymbol{A_{in}}$, of the EIs is reduced by a factor of $\boldsymbol{D}$ to form the spacing, $\boldsymbol{A_{out}}$, of the output image array. A geometrical condition described as $\boldsymbol{A_{out}} = \boldsymbol{p}$ and $\boldsymbol{a_{out}} \leq \boldsymbol{p}$ allows for the multiview reconstruction by the superimposed images.This enables the use of multiple subimages to create a desired composited pattern or a continuous networked pattern. Consequently, scalable projected patterns can be created in stereolithographic additive manufacturing. To prove the concept of the integral imaging patterns, Fig. 3B illustrates the synthesised imagery created by digitally interlacing a set of EIs with identical ($\boldsymbol{a}_{in}^{1} = \boldsymbol{a}_{in}^{2} = \boldsymbol{a}_{in}^{3}$) or three decomposed ($\boldsymbol{a}_{in}^{1} \neq \boldsymbol{a}_{in}^{2} \neq \boldsymbol{a}_{in}^{3}$) spatial components. In both cases, the input objects are spatially multiplexed and decoded as the synthetic images via integration in the imaging plane of the lens array. As the illumination sources are incoherent, the intensity distribution of the synthetic images from the lens array can be assumed to be a simple linear superposition of all reduced EIs. The overall surface topologies and cross-sectional intensity profiles of the projected patterns (Fig. 2C) confirm the consistency between the composite patterns created via integral imaging (see Fig. S5-6 in Supplementary Information). This integral imaging with the sparse spacing of decomposed EIs, which is termed compressive integral imaging in this study, can provide considerable benefits when coupled with inexpensive and low-bandwidth display units (see Fig. S7 and the details in Supplementary Information). Considering frequency analysis based on a simple one-dimensional

model assumption (Fig. S7A) and the Nyquist sampling criteria ($\boldsymbol{v_{Nyq}} = 1/2\boldsymbol{L_P}$), a large display bandwidth ($\boldsymbol{L_P}$ of ~ 50 μm) can provide sufficient spatial resolution to prevent the aliasing (i.e., spectral overlap) in integral imaging with identical and decomposed EIs (Fig. 2C). However, a low bandwidth display unit with an $\boldsymbol{L_P}$ of ~ 220 μm results in aliasing in the integral imaging of identical EIs (Fig. S6B-i) owing to insufficient spatial resolution. Herein, the use of compressive integral projection to decompose the high-frequency spatial component of the initial target image can provide a solution restoring the desired target image (Fig. S7B-ii). Eventhough the integral projection of only three decomposed EIs is used to create the desired target image, we expect that further optimal solutions may be obtained by addressing the inverse problem that arises when low bandwidth subimages are used to synthesise high bandwidth images.

Furthermore, we extend the printing capability of integral lithography to fabricate complex deterministic lattices with chiral or nonperiodic features through the rotational overlapping or stacking of multiple integral projections with controlled angular offsets. Along with the predictable outcomes of rotationally superimposing periodic lattices, deterministic aperiodic structures can reproducibly create specific potential landscapes whose Fourier components are determined by the underlying aperiodic sequence. Furthermore, we demonstrate sophisticated incommensurate aperiodic lattices by overlapping or stacking the periodic integral projections of different dynamic images or different angular offsets. We utilise the rotational stereolithographic configuration that employs an arbitrary, $\boldsymbol{N}$, of repeated exposures as a method for fabricating scalable aperiodic structures. The method is inspired by the mathematical concept of Penrose tiling [42], which generates quasicrystalline tilings through the superposition of distinct grids. This approach enables us to fabricate complex deterministic aperiodic lattice structures by controlling the integral imaging patterns and their angular offsets at each exposure. Figure 2D shows the representative aperiodic lattices including quasicrystalline lattices (quasilattices) with rotational symmetry (i), superlattices with non-equiangular offsets (ii, iii), and incommensurate lattices with no quasiperiodicity or superperiodicity (iv) (see more detailed results in Supplementary Information). Depending on the rotation angle, the printed lattices may have different aperiodic structures without translational periodicity, but they exhibit the rotational symmetry of the sublattices. Additionally, the structures can transform into quasicrystals with higher rotational symmetry or aperiodic albeit regular symmetry (i.e. lattice-dependent symmetry breaking). Therefore, the structures are a promising tool for exploring the physics of wave transport and controlling the properties of wave patterns, which are relevant to several areas of acoustic metasurfaces [34], wave localisation [39, 40], tunable multiband responses of quasilattice metasurfaces [41], and chiral structures [35].

Scalable photopolymerization: The coupling of digitally controlled integral imaging patterns with a lens array allows for the scalable microprinting of various structures. Intertwined fibrous lattice microstructures are printed using Lens 1 with a minimum feature size of ~ 5 μm over an exposure area of up to 2500 mm^2 (Figs. 4A-C and S1E-H). Arbitrary patterns comprised of array lines (Fig. 4F-K) with feature sizes down to 1–2 μm and the array letters of 'MiT' with a length of 50 μm are fabricated using Lens 3 (defined in the caption of Fig. 4 and the Methods section). Considering an exposure area of several square milimetres and a lateral feature size similar to that of the single-aperture imaging-based PμSL configuration [11, 12], the areal ratio ($\sim 10^2$) of printing scales demonstrates that this imaging approach can be scaled without reducing optical resolution. Furthermore, the proposed integral lithography technique provides new opportunities in applications that require the high-throughput fabrication of custom-shaped microparticles or micro-textured surfaces. For example, flexible multiarm particles (Fig. 4D), micro-wavy patterned surfaces (Fig. 4E), or 3D microparticles with microwell arrays (Figs. 4J-K) can be fabricated to serve as customised microstructural platforms for efficient cell-capture in the detection and characterisation of circulating cells [37, 42]. In particular, the integral stereolithographic approach combined with rotational layer-by-layer stacking will be suitable for the scalable fabrication of a distinct class of 3D woodpile lattice structures for Weyl phononic structures [43, 44], or chiral structures [45, 46]. Owing to the strong geometrical correlation between microscale lattices and rotational displacements, microscale geometries can be predicted in structures generated through the 3D rotational stacking of multiple periodic lattices. Figure 3L illustrates the projection view of 3D woodpile lattices printed using Lens 2 via the rotational stacking of parallel rods with different angular offset sequences. Each layer is rotated by an angle of $2\pi/\boldsymbol{N}$ with a linear angular sequence (Fig. 3L(i)-(iv)) or a nonlinear angular sequence (Fig. 3L(v)), and periodic (Fig. 3L(i)–(ii)) or aperiodic lattices (Fig. 3L(iii)–(v)) are formed in the $\boldsymbol{x}$-$\boldsymbol{y}$ plane. Depending on the rotation angle, 3D woodpile lattices can be chiral structures (e.g., $\boldsymbol{N} = 3$ for Fig. 3L(i) and $\boldsymbol{N} = 8$ for Fig. 3L(iii)). Moreover, 3D twisted woodpile lattices can lead to deterministic aperiodic structures with broken lattice-dependent symmetry in the $\boldsymbol{x}$-$\boldsymbol{y}$ plane (Fig. 3L(iii)-(v)). Deterministic aperiodic lattices can provide exciting opportunities in studying transport mechanisms such as wave localization phenomena [36]. Based on the predictable features by the interlayer rotation in superimposing of periodic lattices, we expect to observe new unexplored phenomena such as the exotic lattices of chiral or nonperiodic features.

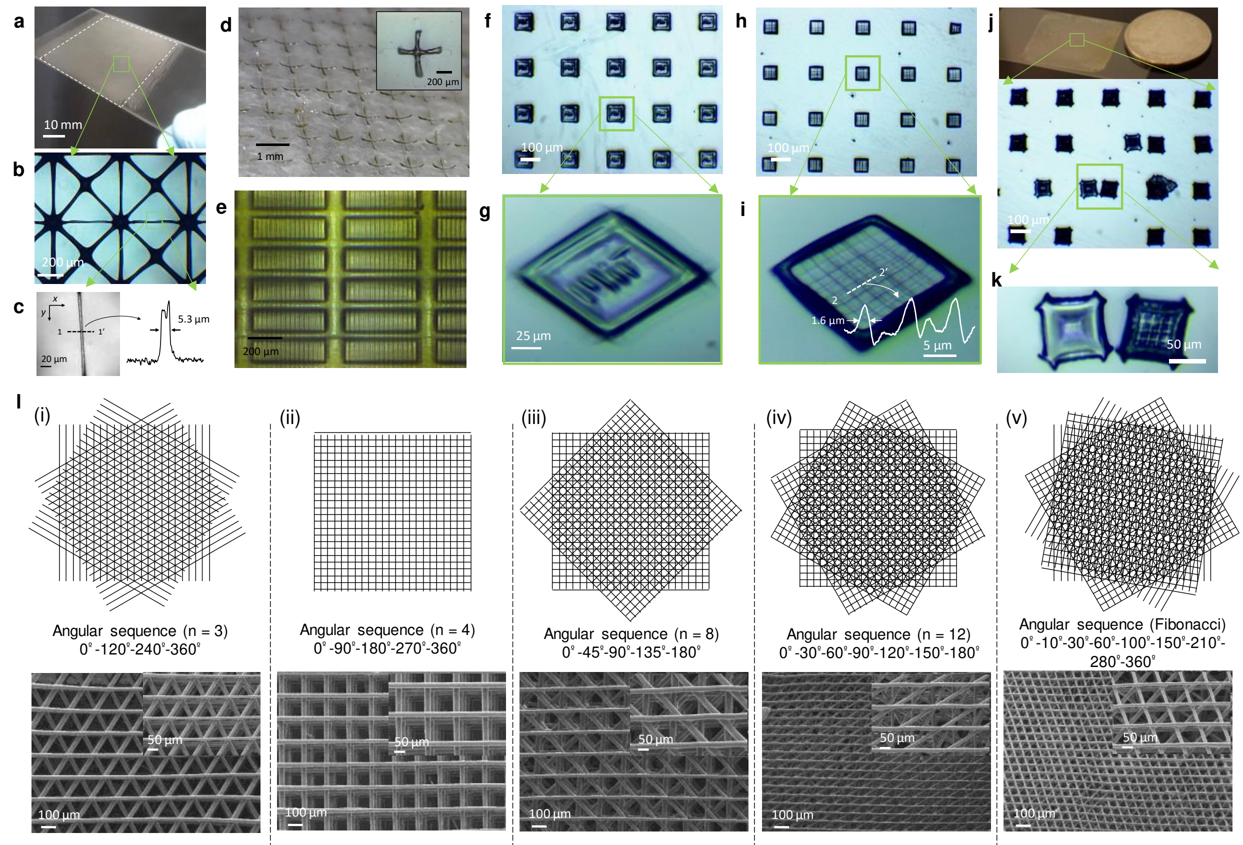

Fig. 3: Scalable printing with small feature sizes. (A–E) Micro-structures/particles created using Lens 1 (***f*** = 5.5 mm, ***p*** = 1 mm, effective ***NA*** of 0.14 in the photopolymer, and an overall size of 50 × 50 mm^2): (A–C) periodic microstructures, such as fibrous lattice, with a minimum feature size of ~ 5.3 μm over an exposure area of up to 2500 mm^2; (D) flexible multiarm microparticles; (E) microtextured surfaces. (F–K) Arbitrary micro-patterns/particles fabricated using Lens 3 (***f*** = 0.57 mm, ***p*** = 0.25 mm, effective ***NA*** 0.33 in the photopolymer, and an overall size of 25 × 25 mm^2): (F–I) Array lines with feature sizes down to ~ 1.6 μm and array letters 'MiT' with a maximum exposure area of up to 625 mm^2; (J–K) 3D microparticles with a microwell array. All microstructures were printed by utilizing the integral imaging patterns of identical EIs with a single exposure of 3–10 s at an intensity of 33 mW/cm^2. The line profiles of the optical images shown in (C) and (I) were quantitatively analysed using the ImageJ software. (L) 3D woodpile lattices with a (i–iv) linear or (v) nonlinear angular sequence, forming (i, ii) periodic or (iii, v) aperiodic structures in the ***x-y*** plane. Depending on the rotation angle, 3D twisted woodpile lattices can be chiral

structures (e.g. N = 3 for (i) and N = 8 for (iii)). 3D woodpile structures were printed using Lens 2 (f = 5.2 mm, p = 0.15 mm, effective NA of 0.021 in the photopolymer, and an overall size of 10 × 10 mm^2).

Discussion

In single-aperture imaging systems based on a pixelated digital microdisplay [47], the areal build size (A_S) during unit exposure is defined as $(total\ pixels) \cdot (\boldsymbol{L_D}/\boldsymbol{M})^2$ (in square milimetres), where L_D is the display pixel size of the constituent digital microdisplay and L_D/M is equal to L_P. A rational strategy for improving resolution is to increase M to decrease L_D. However, reducing L_D by utilising a 10× magnification lens (i.e. M = 10) will decease A_S by 100 times. Thus, the scaling problem of increasing A_S without decreasing resolution remains a challenge in PμSL. To investigate the effect of the integral lithographic system on the scaling issue, we analysed A_S and the minimum feature size (R) for a range of existing PμSL products with available digital microdisplay devices. On the A_s - R plot shown in Fig. 4, R is rendered as $(\boldsymbol{L_D}/\boldsymbol{M})$ [48, 49]. The figure also shows the scaling limit, which is the ability of existing projection-based 3D printing technologies to scale microstructures. The empirical scaling behaviour is deduced from the published specifications of PμSL machines (grey square dots in Fig. 4). The relationship $\boldsymbol{A_S} = \boldsymbol{k} \cdot \boldsymbol{R}^2$ is obtained based on theoretical analysis by following the apparent scaling dependence of the PμSL approach. k is the scaling constant corresponding to the total pixels within available digital microdisplay devices [50-52], and it refers to the SBP in the optical imaging system. In Fig. 4, these analytic scaling boundaries are denoted by dashed lines, where the red and green circles represent the experimental and calculation results obtained for the proposed printing system, respectively. The scaling constant for the relationship between the areal build size (A_I) of integral lithography and the minimum feature size is different from the scaling constant for the A_S–R

relationship for PμSL. Based on the empirical illumination distribution in our system, the achievable maximum condition can be described as $\boldsymbol{A_I} \leq \boldsymbol{A_S}$ because the uniform illumination region and its resulting $\boldsymbol{A_S}$ are determined by the maximum area of the virtual imaging mask to be observed by the lens array [53]. Considering this condition, we estimate the $\boldsymbol{A_S}$–$\boldsymbol{R}$ relationship for integral lithography to compare its performance with that of PμSL as shown in Fig. 4. The effective planar resolution, $\boldsymbol{R_{eff}}$ of the lens array is assumed as $\boldsymbol{R} \times \boldsymbol{D}$ by considering geometric optics. The corresponding equation can be interpreted as

$$\boldsymbol{A_I} \leq \boldsymbol{A_S} = \boldsymbol{k} \cdot \boldsymbol{R}^2 = \boldsymbol{k} \cdot \left(\frac{\boldsymbol{R_{eff}}}{\boldsymbol{D}}\right)^2 = \left(\frac{\boldsymbol{k}}{\boldsymbol{D}^2}\right) \cdot \boldsymbol{R_{eff}}^2 = \boldsymbol{k_{eff}} \cdot \boldsymbol{R_{eff}}^2, \tag{1}$$

where $\boldsymbol{k_{eff}}$ is $\boldsymbol{k}/\boldsymbol{D}^2$ and $\boldsymbol{R_{eff}}$ must be compliant with the Abbe diffraction-limited spot size, $\boldsymbol{d} = 1.22\lambda / 2\boldsymbol{NA}$ [54], where the $\boldsymbol{NA}$ of the unit-lens is defined by $\boldsymbol{n}\sin(\tan^{-1}(\boldsymbol{p} / 2\boldsymbol{f}))$. We assume that the refractive index, $\boldsymbol{n}$, of the photopolymers is 1.5. All printing experiments are performed at an imaging distance, $\boldsymbol{b}$, of 68.75 mm. Additionally, the demagnification factors, $\boldsymbol{D}$, for Lens 1, Lens 2, and Lens 3 are 0.087, 0.082, and 0.0084, respectively, after considering the geometric condition of the lens array. The ideal $\boldsymbol{k_{eff}}$ for Lens 1, Lens 2, and Lens 3 is calculated as 1.35×10^8 (~ 0.14 Gpx), 0.19×10^8 (19 Mpx), and 4.67×10^9 (4.67 Gpx), respectively (the details are provided in the Methods section). Furthermore, we obtain an experimental $\boldsymbol{k_{eff}}$ of 1×10^8 (0.1 Gpx), 0.71×10^6 (0.71 Mpx), and 2.77×10^8 (~ 0. 28 Gpx) for Lens 1, Lens 2, and Lens 3, respectively, based on the printed results. As marked on the upper-left side of the lines that represent the theoretical scaling plot in Fig. 4, our approach demonstrates the potential to overcome the conventional scaling behaviours of the $\boldsymbol{A_S}$–$\boldsymbol{R}$ relationship (SBP–$\boldsymbol{R}$ plot is shown in Fig. S8). However, we believe that the discrepancy between the calculated and experimental $\boldsymbol{k_{eff}}$ does not imply a fundamental limit in the performance of our system. This is because the limit of $\boldsymbol{A_I}$ depends on the available size of the lens array and digital microdisplay devices. Additionally, the obtainable minimum feature size, $\boldsymbol{R_{eff}}$, is determined by overall contribution from photopolymerisation kinetics [11] and the performance of the imaging system (e.g. the effective $\boldsymbol{NA}$ of the available lens array).

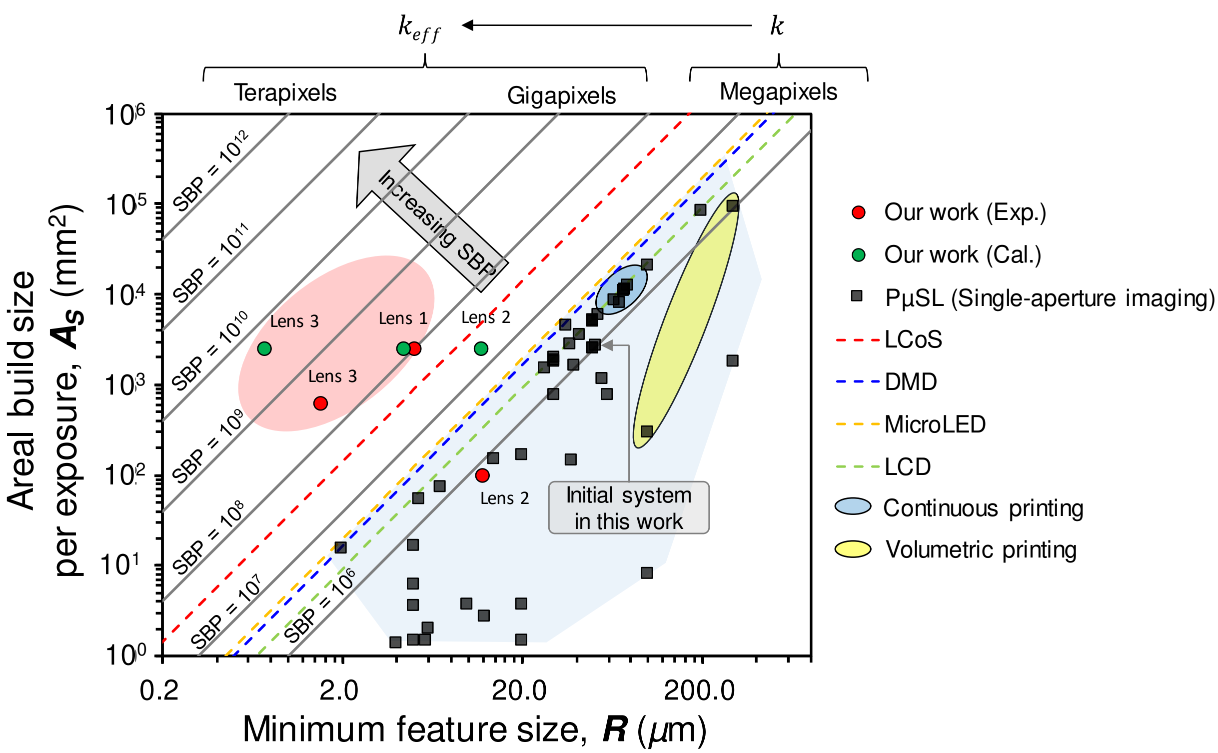

Fig. 4: Figure of merit for the integral lithographic system. Comparison of the PμSL methods as a function of the areal build size ($\boldsymbol{A_S}$) versus the achievable minimum feature size ($\boldsymbol{R}$). The dashed line represents analytical scaling equations grouped by the following digital microdisplay devices: liquid crystal on silicon (LCoS) [49], DMD [50], microLED [51], or liquid crystal display (LCD) [52]. The data points are plotted using the published results for PμSL (based on a single-aperture imaging system) exhibit an empirical scaling dependency. The comprehensive data set used to produce the plot is provided in Table 1 and Fig. S8 in the Supplementary Information. The red and green circles represent the experimental and the calculation results obtained by the authors, respectively, to determine the potential of integral lithography.

Continuous printing [13]; Volumetric printing [19, 20].

We envision that the proposed approach will be used to expand the capabilities of fabricating periodic or deterministic aperiodic microstructures with large areas and mechanical and structural benefits that are yet to be fully utilised at practical scales in volume production applications. If such microarchitectures are made accessible at scales larger than those that currently exist, architected materials, such as those described in this paper, could have widespread applications, e.g. biomedical devices [4], extraordinary mechanical systems [31], functional textured surfaces [33], substrates for energy conversion systems [29, 32], and metastructures for wave engineering [34-36, 39-41, 43-46]. Moreover, our integral lithographic system could be incorporated into other digital light-processing-based lithography systems with different types and sizes of display systems to increases the build areas of the systems further using simple and inexpensive components. This compatibility may motivate the integration of our approach with digital optofluidic fabrication for high-throughput microparticle synthesis [55]. In summary, our work not only provides a scalable stereolithographic microfabrication platform for periodic or deterministic aperiodic printing, but also provides new possibilities for the mass production or large-scale fabrication of microstructures/particles.

Methods

Printing experiment: The integral lithographic system was implemented by modifying the optical platform in a conventional PμSL system comprised of a DMD-based digital microdisplay with a 405-nm LED source (Wintech PRO4500), delivery optics, an optical diffuser (Thorlabs, DG100X100-1500), and the lens array, as shown in Fig. 1A. Note that the initial conditions of $\boldsymbol{R}$

and $\boldsymbol{A_S}$ for the PμSL machine used in this work were ~ 50 μm and 2.56 × 10^3 mm^2, respectively. According to the relationship $\boldsymbol{A_S} = \boldsymbol{k} \cdot \boldsymbol{R}^2$, $\boldsymbol{k}$ was calculated to be 1.04 × 10^6. We employed three types of lens arrays with different focal lengths and larger overall sizes to investigate the scalable integral lithography process. These lenses were denoted as Lens 1 (RPC Photonics, MLA-S1000-f5.5, $\boldsymbol{f}$ = 5.5 mm, $\boldsymbol{p}$ = 1 mm, effective $\boldsymbol{NA}$ of 0.14 in the photopolymer, and an overall size of 50 × 50 mm^2), Lens 2 (Thorlabs, MLA150-5C, $\boldsymbol{f}$ = 5.2 mm, $\boldsymbol{p}$ = 0.15 mm, effective $\boldsymbol{NA}$ of 0.021 in photopolymer, and an overall size of 10 × 10 mm^2), and Lens 3 (Flexible Optical B.V., APO-P(GB)-P250-F0.57, $\boldsymbol{f}$ = 0.57 mm, $\boldsymbol{p}$ = 0.25 mm, effective $\boldsymbol{NA}$ of 0.33 in the photopolymer, and an overall size of 25 × 25 mm^2). The ideal $\boldsymbol{k_{eff}}$ and $\boldsymbol{R_{eff}}$ for Lens 1 were computed to be 1.35 × 10^8 and 4.35 μm using the relationships $\boldsymbol{k_{eff}} = \boldsymbol{k}/\boldsymbol{D}^2$ and $\boldsymbol{R} \times \boldsymbol{D}$, respectively, where $\boldsymbol{D}$ was 0.087. As the effective planar resolution of Lens 2 ($\boldsymbol{R} \times \boldsymbol{D}$ = 4.10 μm, where $\boldsymbol{D}$ was 0.082) was smaller than the Abbe diffraction-limited spot size (1.22λ / 2$\boldsymbol{NA}$ = 11.76 μm), $\boldsymbol{R_{eff}}$ was considered to be 11.76 μm and the ideal $\boldsymbol{k_{eff}}$ was consequently calculated to be 1.55 × 10^8. In addition, as the effective planar resolution ($\boldsymbol{R} \times \boldsymbol{D}$ = 0.42 μm, where $\boldsymbol{D}$ was 0.0084) was smaller that the Abbe diffraction-limited spot size of Lens 3 (1.22λ / 2$\boldsymbol{NA}$ = 0.74 μm), $\boldsymbol{R_{eff}}$ was considered to be 0.74 μm. Thus, the ideal $\boldsymbol{k_{eff}}$ was calculated to be 4.67 × 10^9 by applying the relationship $\boldsymbol{k_{eff}} = \boldsymbol{A_s}/\boldsymbol{R_{eff}}^2$. For the formation of aperiodic microstructures via rotational stacking, we placed Lens 2 on a motorised rotation stage (Thorlabs, PRM1Z8) to synchronise the angular offsets of the lens array unit and dynamic input images during layer-by-layer printing. The microstructures were printed at an imaging distance, $\boldsymbol{b}$, of 68.75 mm. The photocurable material consisted of 1,6-hexanediol diacrylate (Sigma-Aldrich) with a 2% (w/w) phenylbis (2, 4, 6-trimethylbenzoyl) phosphine oxide (Irgacure 819, Sigma-Aldrich) initiator and a 1-phenylazo-2-naphthol (Sudan 1, Sigma-Aldrich) UV absorber. The concentration of the UV absorber varied from 0.05–0.7% (w/w) (Fig. S12). In addition, we used commercial 3D printing resins (IC142-Investment Resin, Colorado photopolymer solutions) in our implementation of the integral lithographic fabrication system.

Imaging: The input images shown in Fig. 2A and C were created on a diffuser through the digital display of a conventional PμSL system using a DMD-based digital optical engine with an L_D of 7.6 μm, M of ~ 1/6.5, and an A_S of 2.56×10^3 mm^2. The output images created by the lens array were recorded by utilising a microscope digital CMOS sensor (AmScope MU500, sensor pixel width of 2.2 μm) with a 2× reduction lens. For the images shown in Fig. 2A and C, we placed Lens 2 (effective NA of 0.014 in air) at an imaging distance of b = 68.75 mm from the masking plane in our system. The kaleidoscopic interwoven patterns in Fig. 2A were produced by adjusting the projection image shapes and sizes from 0.92–3.66 mm with a D of 0.082. The focal plane of the digital microscope camera coincided with the imaging plane of the lens array ($z = b'$). We arranged identical or decomposed EIs (9 × 9) of the concentric circular grating at a distance, A, of 1.83 mm to characterise the projected patterns shown in Fig. 2C (see the details in Supplementary Information).

Illumination scheme: Increasing the illumination distribution over the lens array is an important factor in achieving scalable photopolymerisation. Integral imaging is particularly beneficial for large-area printing because multiple superimposed array objects increase the area of uniform illuminance, as compared to the smaller region illuminated by a single object. In the proposed configuration, a digital microdisplay device projected dynamic images onto an optical diffuser, which functioned as a virtual and reconfigurable photomask. Then the diffuser scattered the light to produce a near Lambertian profile, which ensured homogeneous illumination in all directions in the lens array plane [25, 27, 28]. The scattered light entered the lens array that is positioned at an imaging distance ***b***. Each lens in the array refocused the light to reduce the size of the images generated by the optical diffuser. The illumination distribution incident on the lens array was investigated using various object image configurations (see Figs. S9–11). For simplicity, we used a circular shape as the virtual input image and assumed that the optical diffuser was an imperfect Lambertian emitter (see Figs. S9–11). This simplification enabled us to employ an adapted form of radiometric analysis (see Figs. S9–11) when comparing the illumination distributions of a single object and an array of objects. Based on these assumptions, we derived the approximated equations of illumination distributions for a single object and an array of objects via radiometric analysis using Cartesian coordinates (the details are provided in Supplementary Information). The calculated and measured illumination distributions for our imaging system are shown in Fig. S9. The illumination distribution was measured without the lens array using a home-built scanner (XY-axis stepping motors), which included an optical powermetre and sensor (Thorlabs, PM100D and S120VC, respectively). To reproduce an illumination environment in which the light was incident immediately below the lens array, the optical power distribution was measured over an area of 50×50 mm^2 and at a step size of 0.5 mm at and imaging distance of 68.75 mm from the projected images (the details are provided in Supplementary Information). The measured results were plotted in the form of a 2D illumination distribution using MATLAB. The illumination distribution of a single circular source exhibited a narrow flat region, which provided limited options for scalability. However, the illumination homogeneity was significantly improved by superimposing array object sources. For example, the sum of the illumination distributions for a square array of 5×3 circular sources is depicted in Figs. S9D–F. The illumination distribution was uniform along the horizontal direction at imaging distance ***b*** from the diffuser. These results indicate that this illumination superposition scheme, along with the integral imaging method, can be used to generate a large-scale and uniform illumination distribution.

References and Notes:

1. Schaedler, T. A. et al. Ultralight metallic microlattices. *Science* **334**, 962-965 (2011).

2. Zheng, X. et al. Ultralight, ultrastiff mechanical metamaterials. *Science* **344**, 1373-1377 (2014).

3. Yu, K., Fang, N. X., Huang, G., & Wang, Q. Magnetoactive acoustic metamaterials. *Adv.Mater.* **30**, 1706348 (2018).

4. Espinosa-Hoyos, D. et al. Engineered 3D-printed artificial axons. *Scientific Reports* **8**, 478 (2018).

5. Zhou, X. & Liu, C. Three-dimensional printing for catalytic applications: Current status and perspectives. *Adv. Funct. Mater.* **27**, 1701134 (2017).

6. Zhu, C. et al. Toward digitally controlled catalyst architectures: Hierarchical nanoporous gold via 3D printing. *Sci. Adv.* **4**, eaas9459 (2018).

7. Soukoulis, C. M. & Wegener, M. Past achievements and future challenges in the development of three-dimensional photonic metamaterials. *Nature Photon.* **5**, 523-530 (2011).

8. Truby, R. L. & Jennifer, A. Lewis, J. A. Printing soft matter in three dimensions. *Nature* **540**, 371-378 (2016).

9. Zhang, Y. et al. Printing, folding and assembly methods for forming 3D mesostructures in advanced materials. *Nat. Rev. Mater.* **2**, 17019 (2017).

10. Burckel, D. B. et al. Fabrication of 3D Metamaterial Resonators Using Self-Aligned Membrane Projection Lithography Fabrication of 3D Metamaterial Resonators Using Self-Aligned Membrane Projection Lithography. *Adv. Mater.* **22**, 3171-3175 (2010).

11. Sun, C., Fang, N., Wu, D. M., & Zhang, X. Projection micro-stereolithography using digital micro-mirror dynamic mask. *Sensors and Actuators A* **121**, 113-120 (2005).

12. Raman, R. et al. High-resolution projection microstereolithography for patterning of neovasculature. *Adv. Healthcare Mater.* **5**, 610-619 (2016).

13. Tumbleston, J. R. et al. Continuous liquid interface production of 3D objects. *Science* **347**, 1349-1352 (2015).

14. Zheng, X. et al. Design and optimization of a light-emitting diode projection micro-stereolithography three-dimensional manufacturing system. *Rev. Sci. Instrum.* **83**, 125001 (2012).

15. Emamia, M. M., Barazandeha, F., & Yaghmaieba, F. Scanning-projection based stereolithography: Method and structure, *Sensors and Actuators A* **218**, 116-124 (2014).

16. Zheng, X. et al. Multiscale metallic metamaterials. *Nature Mater.* **15**, 1100-1106 (2016).

17. Lee, M. P. et al. Development of a 3D printer using scanning projection stereolithography. *Scientific Reports* **5**, 9875 (2015).

18. Kato, J., Takeyasu, N., Adachi, Y., Sun, H., & Kawata, S. Multiple-spot parallel processing for laser micronanofabrication. *Appl. Phys. Lett.* **86**, 044102 (2005).

19. Shusteff, M. et al. One-step volumetric additive manufacturing of complex polymer structures. *Sci. Adv.* **3**, eaao5496 (2017).

20. Kelly, B., et al. Volumetric additive manufacturing via tomographic reconstruction. *Science* **363**, 1075–1079 (2019).

21. Malinauskas, M. et al. Ultrafast laser processing of materials: from science to industry. *Light: Science & Applications* **5**, e16133 (2016).

22. Zhou X. et al. Fabrication of Large-Scale Microlens Arrays Based on Screen Printing for Integral Imaging 3D Display. *ACS Appl. Mater. Interfaces* **8**, 24248-24255 (2016).

23. Stuerzebecher, L., Harzendorf, T., Vogler, U., Zeitner, U. D., & Voelkel, R. Advanced mask aligner lithography: Fabrication of periodic patterns using pinhole array mask and Talbot effect. *Opt. Express* **18**, 19485-19494 (2010).

24. Gonidec, M. et al. Fabrication of nonperiodic metasurfaces by microlens projection lithography. *Nano Lett.***16**, 4125-4132 (2016).

25. Geng, J. Three-dimensional display technologies. *Adv. Opt. Photon.* **5**, 456-535 (2013).

26. Manakov, A., et al. A reconfigurable camera add-on for high dynamic range, multispectral, polarization, and light-field imaging. *ACM Trans. Graph.* **32**, 4 (Proc. SIGGRAPH) (2013).

27. Arai, J., Okano, F., Hoshino, H., & Yuyama, I. Gradient-index lens array method based on real-time integral photography for three-dimensional images. *Appl. Opt.* **37**, 2034-2045 (1998).

28. Xiao, X., Javidi, B., Martinez-Corral, M., & Stern, A. Advances in three-dimensional integral imaging: sensing, display, and applications [Invited]. *Appl. Opt.* **52**, 546-560 (2013).

29. Parra-Cabrera, C., Achille, C., Kuhn, S., & Ameloot, R. 3D printing in chemical engineering and catalytic technology: structured catalysts, mixers and reactors. *Chem. Soc. Rev.* **47**, 209-230. (2018).

30. Melchels, F. P. W. et al. Mathematically defined tissue engineering scaffold architectures prepared by stereolithography. *Biomaterials* **31**, 6909-6916 (2010).

31. Lee, W., Kang, D., Song, J., Moon, J. H., & Kim, D. Controlled unusual stiffness of mechanical metamaterials. *Scientific Reports* **6**, 20312 (2016).

32. Thomas, N., et al. 3D printed triply periodic minimal surfaces as spacers for enhanced heat and mass transfer in membrane distillation. *Desalination* **443**, 256-271 (2018).

33. Ran He R., Wang, S., Andrews, G., Shi, W., & Liu Y., Generation of Customizable Microwavy Pattern through Grayscale Direct Image Lithography. *Scientific Reports* **6**, 21621 (2016).

34. Tang, H., Hollow-Out Patterning Ultrathin Acoustic Metasurfaces for Multifunctionalities Using Soft fiber/Rigid Bead Networks. *Adv. Funct. Mater.* **28**, 1801127 (2018).

35. Wu, Z. & Zheng, Y., Moiré Chiral Metamaterials. *Adv. Optical Mater.* **5**, 1700034 (2017).

36. Renner, M. & Freymann, G. von, Transverse Mode Localization in Three-Dimensional Deterministic Aperiodic Structures. *Adv. Optical Mater.* **2**, 226-230 (2014).

37. Li, L., & Yi1, A. Y. Microfabrication on a curved surface using 3D microlens array projection. *J. Micromech. Microeng*. **19**, 105010 (2009).

38. Fang, F., Hammock, D., Irwin, K., Methods for Calculating Empires in Quasicrystals. *Crystals* **7**, 304 (2017)

39. Hladky-Hennion, A. C., Vasseur, J. O., Degraeve, S., Granger, C., and de Billy, M., Acoustic wave localization in one-dimensional Fibonacci phononic structures with mirror symmetry. J. Appl. Phys. 113, 154901 (2013)

40. Wang, P., et al., Localization and delocalization of light in photonic moiré lattices. *Nature* **577**, 42-46 (2020).

41. Han, J., et al., Rotationally reconfigurable metamaterials based on moiré phenomenon. *Opt. Express* **23**, 17443-17449 (2015).

42. Kim, L. N., Choi, S., Kim, J., Kim, H., & Kwon, S., Single exposure fabrication and manipulation of 3D hydrogel cell microcarriers. *Lab Chip* **11**, 48 (2011).

43. He, H., et al., Topological negative refraction of surface acoustic waves in a Weyl phononic crystal. *Nature* **560**, 61-64 (2018).

44. Chen, T., Jiao, J., Dai, H., and Yu, D., Acoustic Weyl points in a square lattice. *Phys. Rev. B* **98**, 214110 (2018).

45. Thiel, M., Freymann, G. von, and Wegener, M., Layer-by-layer three-dimensional chiral

photonic crystals. *Opt. Lett.* **32**, 2547-2549 (2007).

46. Liu, T., Zheng, S., Dai, H., Yu, D., Xia, B., Acoustic semimetal with Weyl points and surface states. arXiv:1803.04284 (2018).

47. Kang, H., Park, J. H., & Cho, D. A pixel based solidification model for projection based stereolithography. *Sensors and Actuators A* **178**, 223-229 (2012).

48. Yang, W., Yu, H., Liang, W., Wang, Y., & Liu, L. Rapid fabrication of hydrogel microstructures using UV-induced projection printing. *Micromachines* **6**, 1903-1913 (2015).

49. Lazarev, G., Hermerschmidt, A., Krüger, S. & Osten, S. *Optical Imaging and Metrology: Advanced Technologies Ch.1* (Wiley-VCH, Weinheim, 2012).

50. TI DLP 4K Ultra High Definition (UHD) Display Chipset: http://www.ti.com/lit/ml/ssnb002/ssnb002.pdf

51. Zhang, L., Ou, F., Chong, W.C., Chen, Y.J., & Li, Q.M. Wafer-scale monolithic hybrid integration of Si-based IC and III-V epi-layers-A mass manufacturable approach for active matrix micro-LED micro-displays. *J. Soc. Inf. Display* **26**, 137-145 (2018).

52. Epson 3LCD, 3-chip technology: https://epson.com/For-Home/Projectors/Pro-Cinema/PowerLite-Pro-Cinema-4855WU-WUXGA-3LCD-Projector-Kit/p/V11H543120MB

53. Wu, R., Zheng, Z., Li, H., & Liu, X. Optimization design of irradiance array for LED uniform rectangular illumination. *Appl. Opt.* **51**, 2257-2263 (2012).

54. Waldbaur, A., Waterkotte, B., Schmitz, K., & Rapp, B. E. Maskless projection lithography for the fast and flexible generation of grayscale protein patterns. *Small* **8**, 1570-1578 (2012).

55. Goff, G. C. L., Lee, J., Gupta, A., Hill, W. A., & Doyle, P. S., High-Throughput Contact Flow Lithography. *Adv. Sci.* **2**, 1500149 (2015).

Acknowledgments

S.K. and N.X.F. acknowledge support from Multidisciplinary University Research Initiative from the Office of Naval Research for financial support through Grant No. N00014-13-1-0631. N.X.F. acknowledges support by the U. S. Army Research Office through the Institute for Soldier Nanotechnologies at MIT, under Contract Number W911NF-13-D-0001. S.K. acknowledges the National Research Foundation of Korea (NRF) grant funded by the Korea government (MSIT) (NRF-2019R1A5A808320112). Y.T.C. acknowledges the Ministry of Trade, Industry & Energy (MOTIE, Korea) under Industrial Technology Innovation Program (No.20000665) and the Technology Innovation Program (20007064, Realization of air cleaning mobility (HAMA Project) (superHydrophobic Additive Manufactured Air cleaner)) funded by the Ministry of Trade, Industry & Energy (MOTIE, Korea). J.J.H. acknowledges the mentorship and seed grant from the MIT Sandbox Innovation Fund. S.K. acknowledges Zheng Jie Tan and Kyungmin Sung for technical support of the illumination distribution measurement. S.K. acknowledges Jungki Song for proofreading.

Author contributions

S.K. and N.X.F. conceived the idea and directed the research. S.K., J.J.H., and Y.T.C. designed the experiments. S.K. developed the printing system and carried out the experiments. S.K., G.B., and N.X.F. analyzed and interpreted the results. N.X.F. supervised the whole project. S.K., J.J.H., and N.X.F. drafted the manuscript and all authors contributed to the writing of the manuscript.

Competing interests

N.X.F., J.J.H., and S.K. are inventors on an invention disclosure at MIT (case no. 20598; created

May 31, 2018) related to this work. All authors declare that they have no other competing interests.

Figures

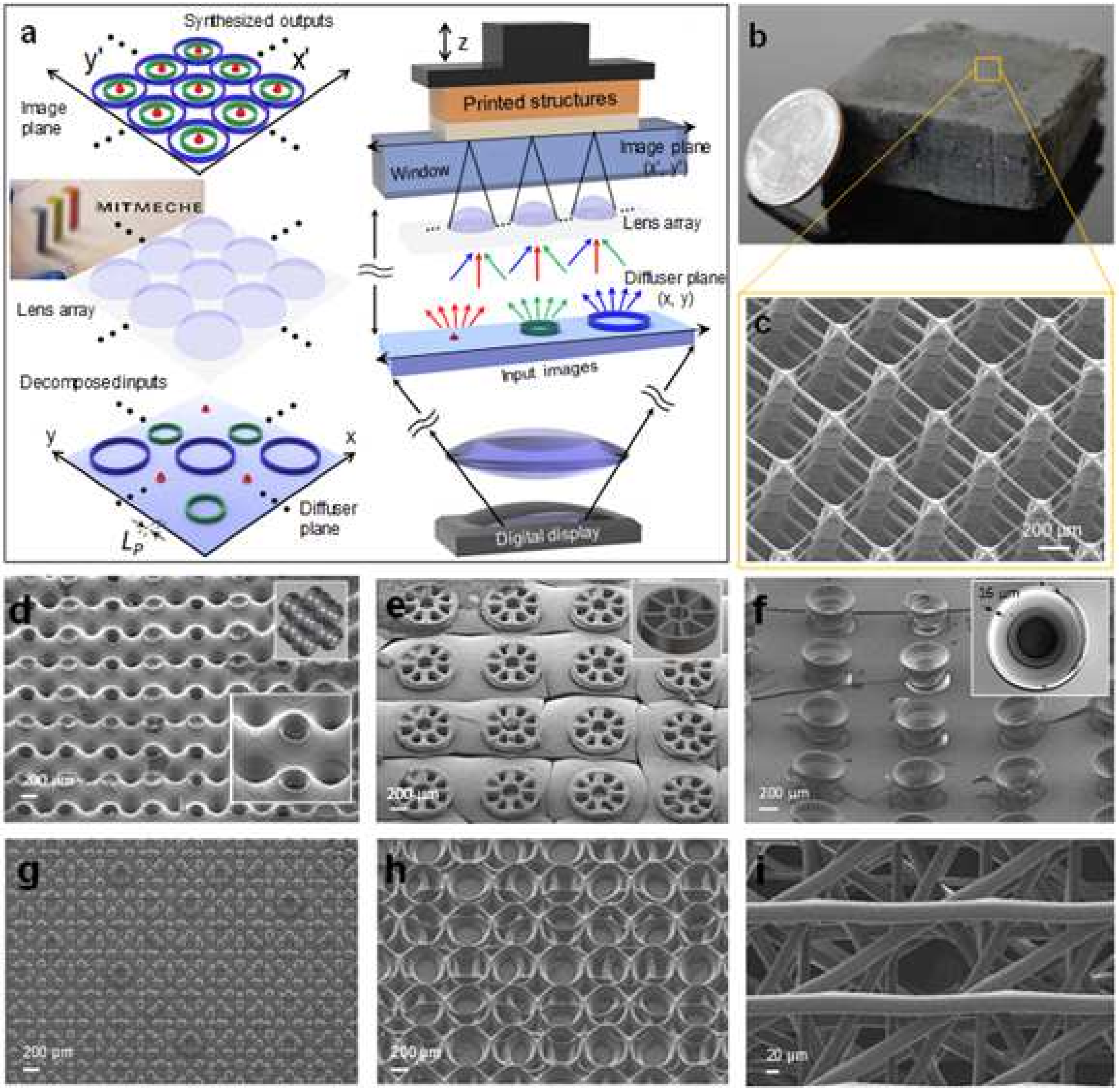

Figure 1

Integral lithographic system for scalable additive manufacturing. (A) Schematic of the integral lithographic system. The reconstructed imaging patterns are projected by the lens array (displayed in front of the MIT mechanical logo) in conjunction with the digital microdisplay. (B to F) Periodic microstructures were fabricated via linear stacking during layer-by-layer printing with an exposure time 3-30 s at an intensity of 33 mW/cm2. These multiscale structures were produced by the lens array (Lens 1, defined in the caption of Fig. 4 and the Methods section): (B) cubic-truss microlattices (400 layers with a polymerisation thickness of 5–50 μm), (C) scanning electron micrograph of microlattices with strut suspended beam diameter of 5 μm; (D) triply periodic bicontinuous structures (60 layers with a polymerisation thickness of 20 μm); (E) circular-lattice microscaffolds (10 layers with a polymerisation thickness of 10 μm); (F) trapezoidal shell-type microstructures with a reentrant geometry (20 layers with a polymerisation thickness of 20 μm). (G to I) Nonperiodic microstructures created via rotational stacking with precisely controllable angular offsets during layer-by-layer printing. These structures were fabricated by a lens array (Lens 2, defined in the caption of Fig. 4 and the Methods section): (G) 8-fold quasi-lattices with hetero sublattices and (H) identical sublattices; (I) deterministic aperiodic woodpile lattices stacked at an angle of 2π/12 with a linear angular sequence.

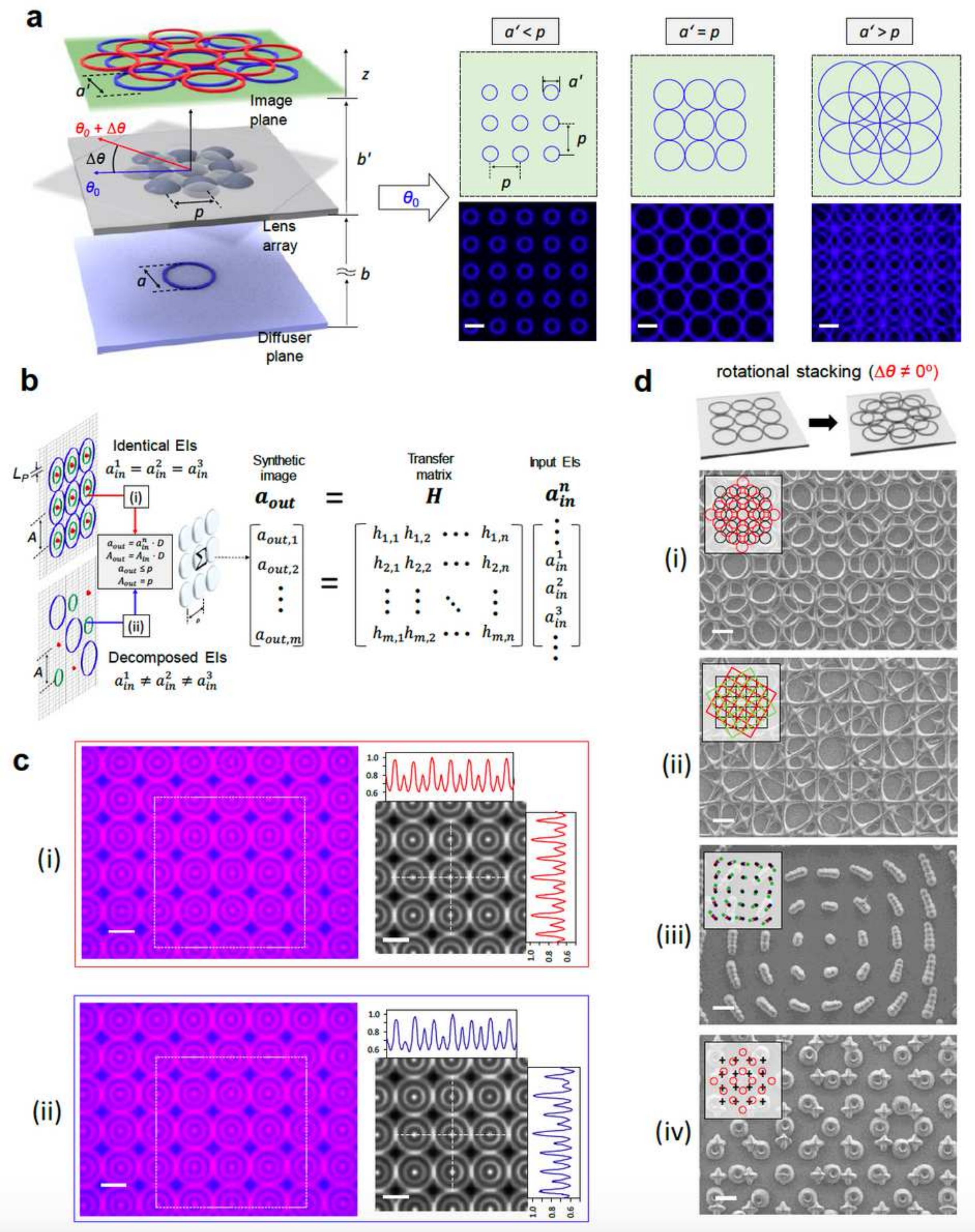

Figure 2

Digitally controlled imaging patterns. (A) The geometric relationship between the lens array and an input object produces kaleidoscopic interwoven patterns. The synthetic images are projected on an imaging plane of the lens array (Lens 2), and captured by an optical microscope. Parallel replication of a single object image by the lens array, which captures an object image and generates an array of repetitive patterns ($a'/p < 1$). Interwoven patterns form through the overlap and superposition of multiple replicated images based on the interaction between the lens array and a single object image ($a'/p \geq 1$). The scale bars are 100 μm. (B to C) Integral imaging patterns with compressive multi-projection: (B) matrix form of the integral image formation between input objects of identical/decomposed EIs and projected outputs. Transfer matrix H is determined by its elements, hm,n, which represent the impulse response function of the unit lens in the lens array. m and n represent the numbers of unit lenses in the lens array in the horizontal and vertical directions, respectively; (C) optical-microscope-captured topologies and cross-sectional intensity profiles of integral imaging patterns created by a digital microdisplay with a projected pixel size (LP) of 50 μm. The intensity profiles were normalised to the maximum grey value versus the pixel distance. (i) and (ii) show integral imaging patterns with the identical EIs and three decomposed EIs, respectively, of the concentric circular grating on the imaging plane through the lens array. (D) Aperiodic lattices with rotational symmetries via multiple integral projections. Broken lattice-dependent symmetry of (i) quasilattices with identical bilayer (angular offset: 45°), (ii-iii) superlattices with identical trilayer (angular offsets: ± 30°) and multilayer (angular offsets: 3°), and (iv) incommensurate Moiré lattices with hetero multilayer (angular offset: 45°). These structures were printed using Lens 2. The scale bars are 100 μm.

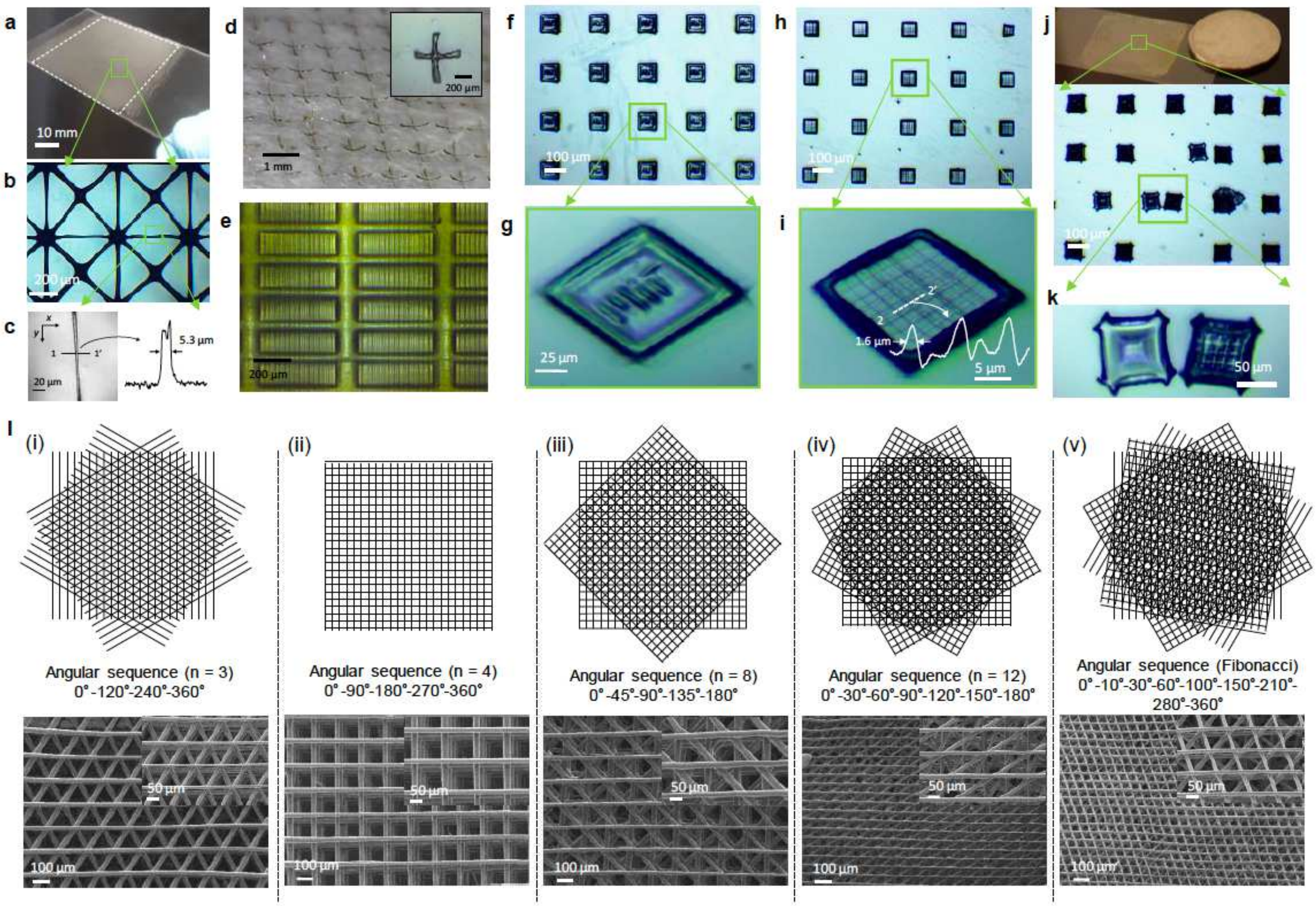

Figure 3

Scalable printing with small feature sizes. (A–E) Micro-structures/particles created using Lens 1 (f = 5.5 mm, p = 1 mm, effective NA of 0.14 in the photopolymer, and an overall size of 50 × 50 mm2): (A–C) periodic microstructures, such as fibrous lattice, with a minimum feature size of ~ 5.3 µm over an exposure area of up to 2500 mm2; (D) flexible multiarm microparticles; (E) microtextured surfaces. (F–K) Arbitrary micro-patterns/particles fabricated using Lens 3 (f = 0.57 mm, p = 0.25 mm, effective NA 0.33 in the photopolymer, and an overall size of 25 × 25 mm2): (F–I) Array lines with feature sizes down to ~ 1.6 µm and array letters 'MiT' with a maximum exposure area of up to 625 mm2; (J–K) 3D microparticles with a microwell array. All microstructures were printed by utilizing the integral imaging patterns of identical EIs with a single exposure of 3–10 s at an intensity of 33 mW/cm2. The line profiles of the optical images shown in (C) and (I) were quantitatively analysed using the ImageJ software. (L) 3D woodpile lattices with a (i–iv) linear or (v) nonlinear angular sequence, forming (i, ii) periodic or (iii, v) aperiodic structures in the x-y plane. Depending on the rotation angle, 3D twisted woodpile lattices can be chiral structures (e.g. N = 3 for (i) and N = 8 for (iii)). 3D woodpile structures were printed using Lens 2 (f = 5.2 mm, p = 0.15 mm, effective NA of 0.021 in the photopolymer, and an overall size of 10 × 10 mm2).

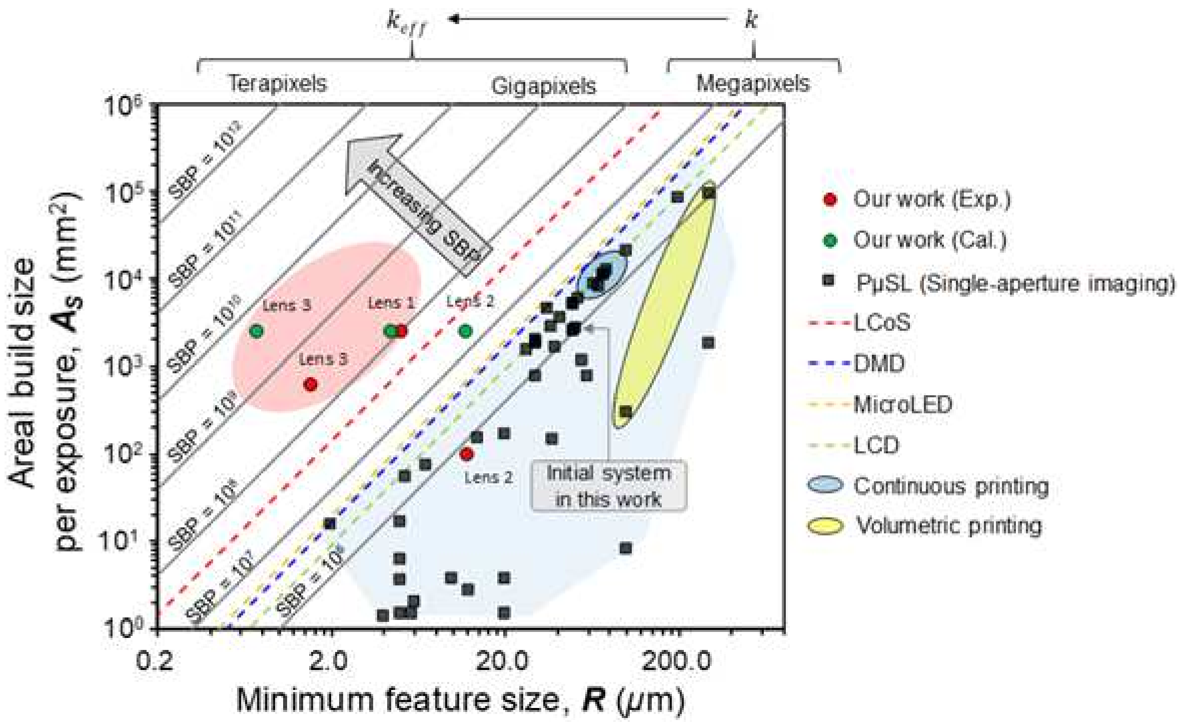

Figure 4

Figure of merit for the integral lithographic system. Comparison of the PμSL methods as a function of the areal build size (AS) versus the achievable minimum feature size (R). The dashed line represents analytical scaling equations grouped by the following digital microdisplay devices: liquid crystal on silicon (LCoS) [49], DMD [50], microLED [51], or liquid crystal display (LCD) [52]. The data points are plotted using the published results for PμSL (based on a single-aperture imaging system) exhibit an empirical scaling dependency. The comprehensive data set used to produce the plot is provided in Table 1 and Fig. S8 in the Supplementary Information. The red and green circles represent the experimental and the calculation results obtained by the authors, respectively, to determine the potential of integral lithography. Continuous printing [13]; Volumetric printing [19, 20].

Supplementary Files

This is a list of supplementary files associated with this preprint. Click to download.

- 215670supp208212qgt11m.docx